Diameter limitations of microsphere and microbottle WGM microresonators fabricated using a low-cost fusion splicer

S. MOHD FARID[1,2], N. A. MOHD YAHAYA[1,2], S. N. F. AZAHAN[1,2], M. K. MOHD YUSOF[1,2], M. Z. ZULKIFLI[1,2,*]
[1]*IIUM Photonics and Quantum Research Centre (iPQC), Department of Physics, Kulliyyah of Science, International Islamic University Malaysia, Bandar Indera Mahkota, 25200 Kuantan, Pahang, Malaysia*
[2]*Physics Department, Kulliyyah of Science, International Islamic University Malaysia, 25200 Kuantan, Pahang, Malaysia*

This study investigates the diameter limitations and performance boundaries of microsphere and microbottle whispering gallery mode (WGM) microresonators fabricated using a low-cost fusion splicer. Diameter is a critical parameter governing mode confinement, free spectral range (FSR), and quality factor (Q), yet its practical limits under arc-discharge fabrication remain insufficiently explored. Both resonator types were fabricated from standard single-mode fibers using controlled electrical discharges and characterized via tapered fiber coupling. Microspheres are found to be constrained by thermal equilibrium, exhibiting saturation at 258.8 μm beyond 30 arc discharges, with high reproducibility (R^2 = 0.9657 and SD = 2.0 μm), a maximum Q-factor of 18,894, and an FSR of 2.44 nm. In contrast, microbottle resonators demonstrate linear and controllable radial growth to a maximum of 232.5 μm on the 50th discharges (R^2 = 0.9723), accompanied by reduced variability (SD from 4.84 μm to 0.97 μm). However, their diameter is ultimately limited by mechanical failure beyond 50 discharges. The microbottle geometry also exhibits axial contraction to 484.8 μm due to surface-tension-driven redistribution, resulting in a lower Q-factor (13,843) and narrower FSR (1.40 nm), while enabling enhanced axial mode control. These findings identify distinct limiting mechanisms which are thermal saturation for microspheres and structural failure for microbottles, providing a practical framework for optimizing WGM resonator design within low-cost fabrication environments.

(Received September 28, 2025; accepted June 2, 2026)

Keywords: Whispering Gallery Mode (WGM) Microresonators, Microsphere, Microbottle, Fiber Fusion Splicer, Quality Factor (Q) and Free Spectral Range (FSR)

1. Introduction

Whispering gallery mode (WGM) microresonators are compact optical cavities that confine light along a curved dielectric interface via total internal reflection, enabling strong optical field enhancement, ultrahigh quality (Q) factors, and ultralow mode volumes [1]. In these structures, light circulates along the periphery of the resonator and constructively interferes when the optical path length satisfies the resonance condition [2]:

$$m\lambda=2\pi nR \quad (1)$$

where m is the azimuthal mode number, λ is the resonant wavelength, n is the refractive index of the resonator material, and R is the resonator radius. This resonance condition forms the physical basis of WGM confinement and determines the discrete spectral modes supported by the resonator. Due to the long photon lifetime and strong optical confinement within these cavities, WGM resonators are highly attractive for sensing, nonlinear optics, optoelectronics, and microlaser applications, where small environmental perturbations induce measurable spectral shifts [3].

WGM resonators have been realized in various geometries, including microspheres, microbottles, microtoroids, and microdisks [4]. Among the various WGM geometries, microspheres and microbottles are selected in this work because both can be fabricated directly from standard silica optical fibers through surface-tension reshaping using arc-discharge heating [5,6]. In contrast, microtoroids and microdisks require lithographic patterning and cleanroom processing, resulting in substantially higher cost and fundamentally different fabrication constraints [7]. Since this work investigates diameter limitations imposed specifically by low-cost fusion splicer processing, only geometries compatible with this platform are considered. This approach ensures experimental consistency and directly addresses the needs of laboratories operating under budget constraints.

Microspheres represent the fundamental benchmark WGM geometry due to their rotational symmetry and well-established theoretical description [8]. In these structures, the optical field is confined near the equatorial plane, where total internal reflection maintains the circulating optical modes [8]. The optical modes decay evanescently outside the resonator surface, allowing external coupling through a tapered optical fiber placed within the evanescent field region [9]. Efficient coupling occurs when the propagation constant of the tapered fiber mode matches the effective propagation constant of the WGM circulating inside the resonator [9]. Under this phase-matching condition, optical power can be transferred between the fiber and the resonator, enabling excitation and detection of the resonant modes [10].

Microbottle resonators, while fabricated from the same fiber platform, introduce axial radius variation and additional longitudinal confinement [11]. Unlike microspheres, which support only azimuthal modes, microbottles support both azimuthal and axial modes due to the gradual variation in radius along the fiber axis [11]. This axial confinement creates a harmonic potential for light propagation, leading to the formation of discrete axial resonances [12]. Comparing these two structures therefore enables a controlled and physically meaningful investigation of geometry-dependent diameter effects within a single fabrication framework.

Resonator diameter is a primary parameter governing optical performance. The free spectral range (FSR), which represents the wavelength spacing between adjacent resonances, is inversely proportional to the resonator radius and can be expressed as [13]:

$$\mathrm{FSR} \approx \frac{\lambda^2}{2\pi n R} \tag{2}$$

where R is the resonator radius and n are the refractive index of the resonator material. This relationship shows that smaller resonators exhibit larger spectral spacing, while larger resonators produce more closely spaced resonant modes. The resonator diameter also influences the optical quality factor Q, defined as [14]:

$$Q = \frac{\lambda}{\Delta\lambda} \tag{3}$$

where $\Delta\lambda$ is the resonance linewidth. The Q factor represents the photon storage capability of the resonator and is strongly affected by radiation loss, surface scattering, and material absorption [14]. In addition, the optical mode volume V_m, which characterizes the spatial confinement of the optical field, scales approximately with the square of the resonator radius [15].

Thus, resonator diameter fundamentally determines spectral spacing, confinement strength, radiation loss, and overall resonator stability [16]. Thus, the “diameter limitation” refers to the minimum and maximum resonator diameters achievable using arc-discharge fusion splicing while maintaining structural integrity and measurable WGM performance. At small diameters, excessive curvature leads to increased radiation loss and Q degradation while at large diameters, fabrication stability and repeatability become limiting factors [17]. Despite its importance, the practical diameter range attainable using affordable fusion splicers remains insufficiently explored.

In this work, microsphere and microbottle resonators are fabricated using a low-cost fusion splicer under controlled arc-discharge conditions. Their geometrical limitations will be examined in order to determine the practical diameter range achievable through the fusion-splicing fabrication process. Among the fabricated structures, resonators with the largest stable diameters will be selected for tapered fiber coupling, since larger provide stronger optical confinement and more stable whispering gallery modes due to reduced curvature-induced radiation losses, which enables higher achievable Q factors and narrower resonance linewidths. These resonators will subsequently be characterized using tapered fiber coupling to evaluate their optical performance, including the free spectral range (FSR), quality factor (Q), and coupling characteristics. The findings contribute to the development of accessible WGM microresonator platforms by establishing the practical diameter limits and Q-factor achievable using low-cost fusion-splicing techniques, thereby enabling wider adoption of high-performance optical resonators in resource-limited research environments.

2. Experimental setup

2.1. Fabrication of microresonators

The microsphere and microbottle resonators were fabricated using a core-to-core fusion splicer (ACUTEQ ATS-A6). The splicer generates a localized electric arc between electrodes, producing controlled heating that softens the silica fiber. Upon cooling, surface tension reshapes the molten region into a smooth three-dimensional geometry, enabling the formation of fiber-based microresonator without cleanroom processing as seen in Fig. 1.

Prior to fabrication, fibers were stripped and cleaned using isopropyl alcohol (IPA) and lint-free laboratory wipes (Kimwipes) to remove dust, organic residues, and other surface contaminants that could affect the quality of the resonator surface. The cleaved fiber ends (4° cleave angle) were aligned and secured in the splicer’s fiber holders. The fabrication process was controlled using two primary splicer functions: the Arc function, which releases electric discharge to heat and soften the fiber, and the **Set** function, which adjusts fiber positioning or fuses fiber ends together.

The splicer was programmed to operate at 45% of the nominal arc power with a discharge duration of 1600 ms (approximately 2 s per Arc press). These parameters were selected based on preliminary optimization trials. Arc powers below 40% resulted in insufficient glass softening and incomplete reshaping, whereas powers above 50% caused excessive deformation and reduced dimensional control. Similarly, discharge durations shorter than 1200 ms produced unstable geometries, while durations exceeding 1800 ms increased surface irregularities and asymmetry. The selected parameters therefore provide an optimized balance between controlled glass reflow, geometric stability, and fabrication repeatability.

Microspheres were formed by applying sequential Arc discharges to the opposing fiber tips without axial pulling. Each Arc press heated the fiber ends, causing symmetrical expansion due to surface tension and gradual formation of spherical tips. The number of Arc discharges was varied between 1 and 35 presses to systematically investigate diameter evolution. The Set function (1 s press) was used once only when necessary to reduce the slight separation between softened tips caused by melting. The final microsphere diameter was controlled exclusively by varying the total number of Arc discharges while maintaining constant arc power and duration. To clearly define the discharge–diameter relationship, the fabrication parameters and corresponding formulas are summarized in Table 1.

Table 1. Discharge parameters and diameter control formula for microsphere resonators

Step	Function	Frequency	Function	Formula
1	Arc	1 to 35	Heats fibre tips to form spherical geometry	$N_{arc} = N_{total}$
2	Set	1	Adjusts gap after melting	—

Thus, the total number of arc discharges used in the microsphere fabrication process is determined by the selected arc discharge frequency cycles, where the cumulative discharge count is represented by $N_{arc} = N_{total}$.

Microbottle resonators were fabricated using a two-stage process. First, 15 Arc discharges were applied to both fiber ends to form enlarged spherical tips. The Set function was then pressed twice to fully fuse the spherical tips into a continuous structure. In the second stage, additional Arc discharges (5 to 35 presses) were applied to the fused region. These repeated discharges reheated the structure, allowing controlled reflow and expansion into a bottle-shaped bulge with tapered neck regions. The bottle diameter and axial length were therefore tuned by adjusting the total number of Arc discharges. The total electric discharge applied to a microbottle corresponds to the cumulative number of Arc presses across both stages. To clearly define the discharge–diameter relationship, the fabrication parameters and corresponding formulas are summarized in Table 2.

Table 2. Discharge parameters and diameter control formula for microbottle resonators

Step	Function	Frequency	Function	Formula
1	Arc	15	Forms spherical tips	$N_{arc,1}$
1	Set	2	Fuses tips together	-
2	Arc	5 to 35	Expands fused region into bottle shape	$N_{arc,2}$

Thus, the cumulative value of arc discharges becomes $N_{total} = N_{arc,1} + N_{arc,2}$, where ($N_{arc,1}$) initial discharges before applying the set function and ($N_{arc,2}$) represents additional discharges applied during bottle formation.

Fig. 1. Formation of microresonators from single-mode fibers using a fusion splicer (colour online)

To evaluate fabrication reproducibility, at least three independent resonators were fabricated for each discharge configuration. All resonators were fabricated under identical laboratory conditions to minimize variability. Post-fabrication, the microresonators were thoroughly cleaned again using isopropyl alcohol (IPA) to remove surface contaminants that could affect the quality of the resonator surface. Surface smoothness and symmetry were inspected optically to confirm uniform reflow and absence of visible defects.

2.2. Geometrical characterization

The geometrical characterization of the fabricated WGM microresonator was performed using a digital upright optical microscope (Nikon platform) equipped with 4×, 10×, and 20× plan objectives and calibrated image analysis software (NIS-Elements D). Diameters were extracted from calibrated micrographs by averaging multiple cross-sectional measurements to reduce edge-detection uncertainty. Mean values with standard deviations (error bars) between samples with the same arc discharges were calculated to assess consistency.

Fig. 2 presents the geometrical parameters used to characterize the fabricated whispering gallery mode (WGM) resonators. Two types of fibre-based resonators were analyzed: (a) a microsphere resonator and (b) a microbottle resonator. For the microsphere structure (Fig. Xa), the primary geometrical parameter is the sphere diameter D_s, defined as the maximum transverse dimension of the spherical cavity. In the case of the microbottle resonator (Fig. Xb), two key geometrical parameters were measured: the maximum bottle diameter $D_b$and the axial bottle length L_b, which corresponds to the longitudinal distance between the two transition regions where the fibre begins to expand and contract. These parameters were obtained from optical microscope images using calibrated image analysis to ensure accurate dimensional measurement. The geometrical characterization provides a quantitative basis for correlating the fabricated resonator dimensions with their subsequent optical behavior.

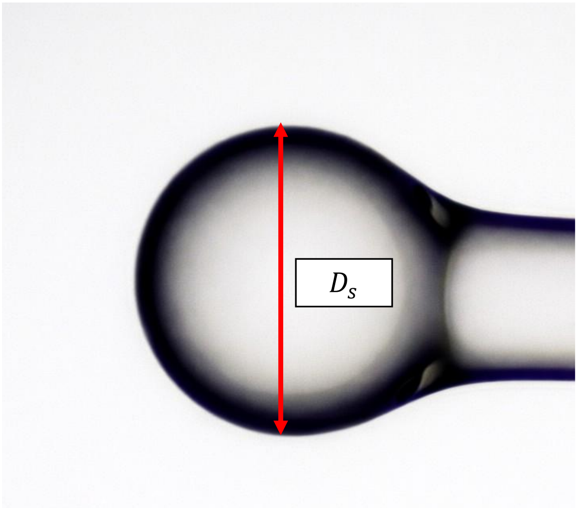

(a)

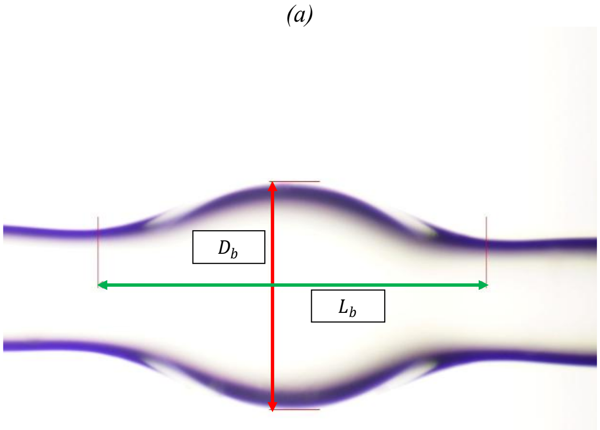

(b)

Fig. 2. Geometrical parameters of fibre-based whispering gallery mode (WGM) resonators fabricated using arc-discharge fusion splicing: (a) microsphere resonator showing the sphere diameter D_s and (b) microbottle resonator indicating the maximum bottle diameter D_b and axial bottle length L_b (colour online)

2.2. Optical characterization and coupling configuration

To systematically evaluate the performance boundaries of the proposed fabrication method, a dual-stage characterization strategy was employed. While the full range of fabricated diameters was monitored under high-resolution microscopy to verify structural integrity and dimensional consistency, detailed optical characterization via tapered fiber coupling was strategically focused on the samples with the largest radial diameters. This sampling strategy is grounded in Whispering Gallery Mode (WGM) theory, which dictates that curvature-induced radiative losses are minimized as the resonator radius increases. By prioritizing these upper-bound dimensions for spectral analysis, this study benchmarks the peak performance potential, specifically the maximum achievable Q-factor, within the identified diameter limitations. This approach ensures that the reported results define the optimal technical envelope of the low-cost fusion-splicing system while maintaining a clear focus on the physical limits of the resonators.

Optical characterization of the fabricated resonators was performed using a tapered fibre coupling configuration, which enables efficient excitation of whispering gallery modes through evanescent field interaction. The experimental setup used for the coupling measurements is illustrated in Fig. 3. Light from a broadband optical source was launched into a tapered optical fibre mounted on precision translation stages, while the fabricated microresonator was positioned within the evanescent field region of the taper to facilitate optical coupling. The transmitted signal was subsequently analyzed using an optical spectrum analyzer (OSA).

The tapered fibres were fabricated using the flame-brushing technique. A 2 cm section of uncoated SMF-28 fibre was mounted on two motorized linear translation stages (Thorlabs, 300 mm range) and symmetrically pulled at a constant speed of 0.4 mm/s. An oxybutane flame was translated along the fibre at a controlled speed of 0.0625 mm/s using a motorized stage powered by a 50 V, 4 A, 175 W supply. The pulling distance and heating profile were carefully calibrated to produce sub-micron waist diameters, which are required to generate strong evanescent fields for efficient coupling to the resonator modes. Subsequently, a taper fibre with a waist of 1.27 µm was fabricated and used for the coupling process.

Prior to coupling with the fabricated microresonators, transmission spectra of the tapered fibre alone were recorded as control measurements to verify that no intrinsic resonant features were present in the fibre. During measurement, the fabricated microresonator was positioned adjacently to the tapered fibre using a precision micropositioning stage, as shown in Fig. 4. The coupling gap was carefully adjusted to achieve near-critical coupling while maintaining mechanical stability. Effective excitation of whispering gallery modes occurs when the resonator is placed sufficiently close to the taper to allow overlap between the evanescent field and the resonator surface.

A C-band erbium-doped fiber amplified spontaneous emission (ASE) source was used as the broadband input, and the transmitted signal was analyzed using an Optical Spectrum Analyzer (OSA203). The resolution bandwidth of the OSA was set to 0.01 nm to ensure that measured full width at half maximum (FWHM) values were not limited by instrumental resolution.

Extracted parameters included resonant wavelength, free spectral range (FSR), full width at half maximum (FWHM), and quality factor, calculated as $Q = \lambda/\Delta\lambda$, where λrepresents the resonant wavelength and $\Delta\lambda$denotes the resonance linewidth (FWHM). The resonant wavelength was determined from the minimum transmission dip in the spectrum, while the FSR was obtained from the spacing between adjacent resonances. The FWHM was measured at the half-maximum (−3 dB) level of the resonance dip by identifying the wavelength difference between the two points corresponding to half of the transmission depth. All spectral parameters were extracted from high-resolution optical spectrum analyzer (OSA) measurements.

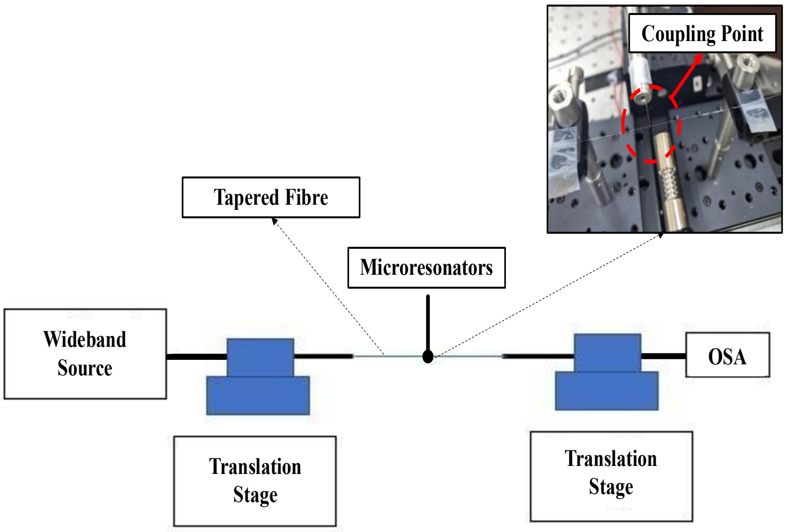

Fig. 3. Experimental setup for WGM optical characterization using tapered fibre coupling. The inset shows the view of the microresonator-taper coupling point using a microsphere (colour online)

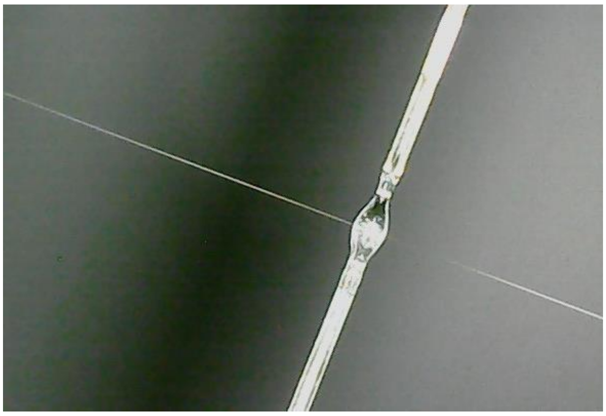

Fig. 4. Optical microscope image of a fibre-based whispering gallery mode (WGM) resonator (microbottle) fabricated using arc-discharge fusion splicing. The tapered fibre positioned adjacent to the resonator enables evanescent coupling for optical characterization (colour online)

3. Result and discussion

3.1. Diameter of microsphere resonators

Fig. 5 illustrates the evolution of the microsphere diameter as a function of the number of electrical arc discharges (N_{arc}). The diameter follows a predictable growth trend, initiated from a minimum mean of 155.3 µm after a single discharge and reaching a maximum mean of 260.9 µm. The high coefficient of determination (R^2 = 0.9657) confirms the excellent controllability of the fabrication process using the low-cost fusion splicer.

The error bars in Fig. 5 represent the standard deviation (SD) calculated from 3 fabrication trials, with values remaining consistently low, ranging from 2.0 µm to 4.8 µm. These narrow error bars demonstrate the high degree of repeatability inherent in the arc-discharge technique, ensuring that the resulting resonator dimensions are consistent across different fabrication cycles.

The experimental data reveals that the rate of diameter enlargement is highest during the initial 15 discharges but becomes stagnant (reaches saturation) beyond the 30th discharge. This saturation phenomenon occurs because the arc discharge which are fixed at 45% of the maximum power for 1600 ms, provides a finite thermal energy input. As the microsphere volume increases, the rate of heat dissipation via conduction through the fiber stem and convection into the surrounding air also increases [18]. Once the thermal energy supplied by the arc reaches an equilibrium state with these cumulative heat losses, the silica remains in a molten state without further expanding. These results demonstrate that while the microsphere size can be precisely regulated, the maximum achievable diameter is physically capped by the thermal equilibrium of the splicing system.

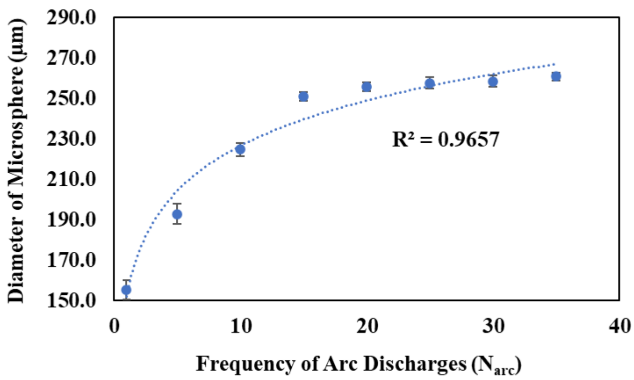

Fig. 5. Microsphere diameter as a function of the number of electrical discharges applied using the fiber fusion splicer (colour online)

3.2. Diameter and axial length of microbottle resonators

Fig. 6 illustrates the average diameter evolution of the fabricated microbottle resonators as a function of the number of electrical arc discharges (N_{arc}). The resonator diameter demonstrates a highly predictable and consistent linear growth, expanding from a minimum mean of 193.5 μm at 20 discharges to a maximum mean of 232.5 μm at 50 discharges. This strong linear correlation, evidenced by an improved coefficient of determination (R^2 = 0.9723), confirms the exceptional precision and controllability of the arc-discharge process using a low-cost fusion splicer.

The error bars in Fig. 6 represent the standard deviation across multiple independent fabrication cycles. Notably, the variance remains consistently low, ranging from a maximum of 4.84 μm at lower discharge counts to a highly stable 0.97 μm as the resonator reaches its maximum dimensions. This minimal variance underscores the high structural reproducibility of the technique, which is a critical factor for maintaining consistent Whispering Gallery Mode (WGM) performance and spectral stability across different fabrication batches.

Beyond 50 discharges, the silica fiber suffers from structural fracture and breakage due to excessive localized thermal stress and overheating. This mechanical failure defines the ultimate "diameter limitation" for this low-cost fusion-splicing technique. Consequently, an optimized range of 45 to 50 discharges was established to maximize the resonator's radial diameter, and thus enhance optical confinement and the Q-factor by increasing the radial diameter, without compromising the structural integrity of the fiber.

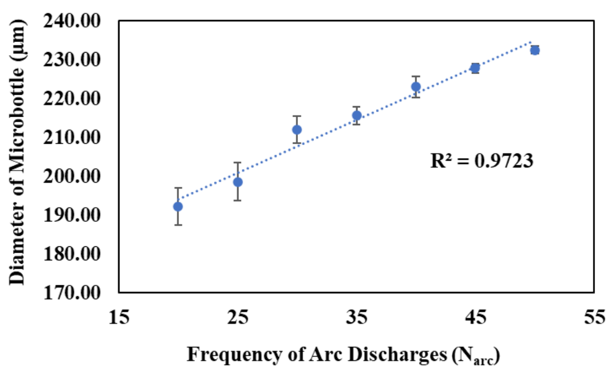

Fig. 6. Microbottle diameter as a function of the number of electrical discharges applied using the fiber fusion splicer (colour online)

Fig. 7 illustrates the evolution of the microbottle axial length as a function of the number of electrical arc discharges (N_{arc}). The fabrication of the microbottle involves the initial formation of two microspheres on adjacent fiber tips, which are subsequently fused together to create the resonant cavity. As the frequency of arc discharges increases from 20 to 50, the average axial length demonstrates a clear and consistent linear decrease, ranging from a maximum mean of 543.2 μm at 20 discharges to a minimum of 484.8 μm at 50 discharges.

The error bars in Fig. 7 represent the moderately high standard deviation (SD) across multiple trials, with values ranging from a maximum of 8.00 μm down to a 2.80 μm as the process stabilizes. The moderate fluctuations and the R^2 value of 0.9141 are primarily attributed to the high-temperature surface tension effects during the fusion process; as more thermal energy is applied through repeated discharges, the molten silica tends to pull inward toward the centre, effectively shortening the axial span of the "bottle" shape.

While the axial length can influence mode localization and radiation losses, its impact is typically secondary to the dominant role of the central diameter [19]. However, this controllable reduction in length is significant for applications in nonlinear optics, as it provides an additional degree of freedom for tuning spectral density and manipulating axial mode structures [20]. Similar to the radial diameter, the axial length reaches a physical fabrication limit at 50 discharges, beyond which the increased thermal stress leads to fiber breakage.

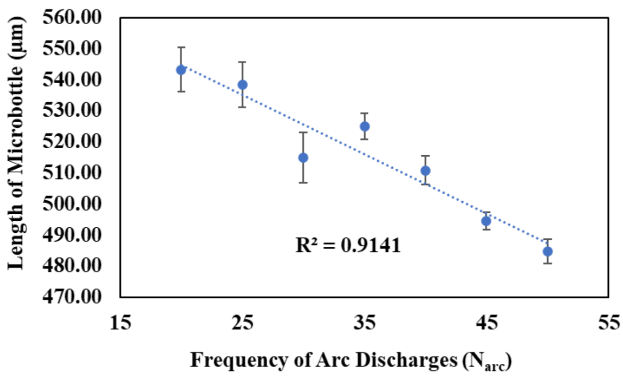

Fig. 7. Microbottle axial length as a function of the number of electrical discharges applied using the fiber fusion splicer (colour online)

3.3. Characterization of microresonators

Fig. 8 presents the transmission spectra before and after coupling the tapered fibre to the microsphere resonator. Upon coupling, the guided light in the tapered fibre evanescently interacts with the resonant modes of the microsphere, allowing optical energy to be transferred into the cavity. At specific frequencies that satisfy the resonance condition of the microresonator, the circulating light constructively builds up within the sphere. This results in distinct dips in the transmission spectrum when the input light frequency matches the resonant frequencies of the whispering gallery modes (WGMs). These resonance dips indicate efficient coupling between the tapered fibre and the microsphere. The enhanced electromagnetic field within the cavity at resonance increases intrinsic losses, such as material absorption and surface scattering, which manifest as reductions in the transmitted intensity. In short, the observed spectral dips correspond to the excitation of WGM resonances in the microsphere cavity. Figure 12 and Figure 13 shows the coupling spectrum of both microbottle and microresonator respectively.

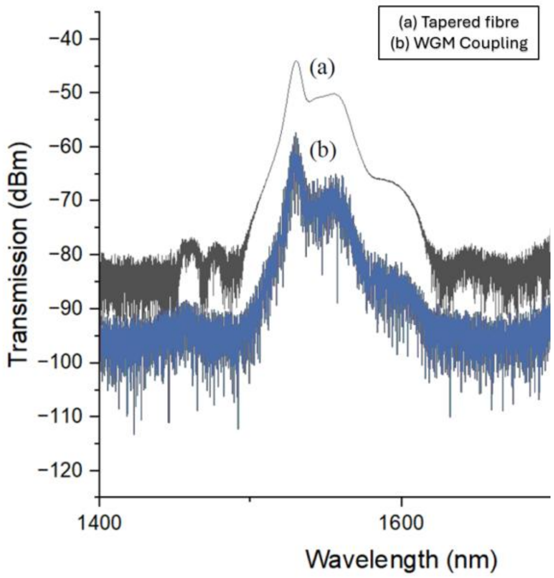

Fig. 8. Transmission spectrum measured (a) Before and (b) After coupling (colour online)

Table 3 summarizes the optical properties of the fabricated microsphere and microbottle with the largest curvature based on the couple spectrum in Fig. 9 and 10. The microsphere resonator showed superior performance, achieving the highest Q factor of 18,894 at 260.96 µm (30 arc discharges). This is significantly higher than the microbottle due to the microsphere's better symmetry and lower scattering losses. It also exhibited a larger FSR of 2.44 nm, providing wider mode spacing and reducing overlap between adjacent modes which is useful for single-mode operation and wavelength selectivity.

The microbottle resonator exhibited a Q factor of 13,843 with a diameter of 232.5 µm (fabricated using 50 arc discharges). The free spectral range (FSR) was lower, at 1.40 nm, compared to the microsphere despite having a smaller diameter. Earlier reports suggest that smaller resonator geometries generally show higher FSR values [21]. This reduction is possibly due to geometry of microbottle itself when fabricated using a fusion splicer. Unlike microspheres, which exhibit nearly perfect symmetry, microbottles possess an elongated axial geometry. As a result, the light does not circulate strictly around the smallest diameter [22]. Instead, depending on the coupling position, the resonant modes can extend along the bottle's axial length, effectively increasing the optical path and leading to a lower FSR [22]. Microbottle resonators are particularly attractive for applications requiring spectral tuning and mode flexibility, despite their lower Q factors.

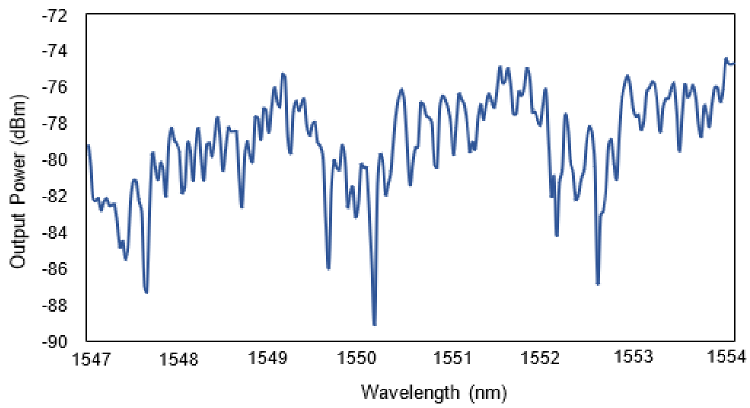

Fig. 9. Coupling spectrum of microsphere resonator (colour online)

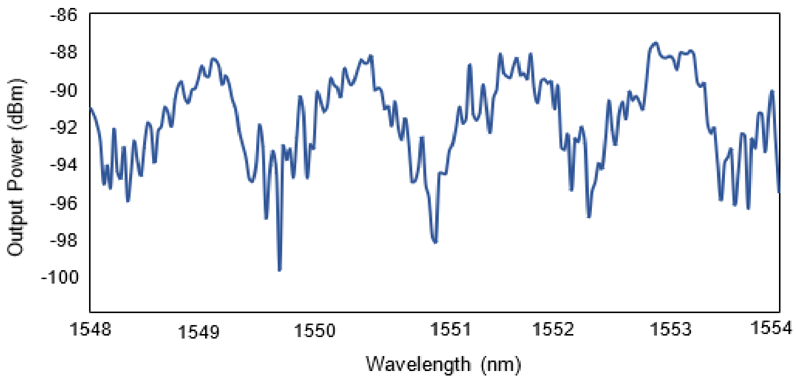

Fig. 10. Coupling spectrum of microbottle resonator (colour online)

Table 3. The optical properties of both microresonators

Properties	Microsphere	Microbottle
Diameter (μm)	260.96	232.50
Axial Length (μm)	-	484.76
Resonant Wavelength (nm)	1550.37	1550.97
FWHM (pm)	82.05	112.04
Q-factor	18894	13843
FSR (nm)	2.44	1.40

3.3. Comparative analysis

A comparative assessment of the fabricated microsphere and microbottle resonators reveals distinct performance trade-offs governed by their respective geometries and the thermal dynamics of the arc-discharge process. While both structures were successfully fabricated using the same low-cost fusion splicing platform, the microsphere demonstrated a superior peak quality factor of 18,894 and a wider FSR of 2.44 nm, compared to the microbottle values of 13,843 and 1.40 nm, respectively. This higher performance in the microsphere is attributed to its near-perfect rotational symmetry, which minimizes scattering losses and radiative leakage. Furthermore, the microsphere growth follows a logarithmic trend that reaches a stable thermal equilibrium beyond 30 discharges ($N_{arc} > 30$), ensuring high structural reproducibility with a standard deviation as low as 2.0 μm.

In contrast, the microbottle introduces a more complex morphological evolution and an additional degree of freedom through its axial length, defining a different set of diameter limitations. Unlike the self-limiting growth of the microsphere, the microbottle diameter demonstrates a highly predictable linear expansion ($R^2 = 0.9723$) until it reaches a hard mechanical failure point at 50 discharges due to localized thermal stress. Simultaneously, the microbottle exhibits a unique dual-axis contraction where the axial length decreases from 543.2 μm to 484.8 μm ($R^2 = 0.9141$) as surface tension pulls the molten silica toward the centre during repeated melting cycles. Despite its smaller radial diameter, the microbottles significantly narrower FSR is a direct consequence of this elongated geometry; the resonant modes extend axially, increasing the effective optical path length and compressing the spectral spacing. Ultimately, while the microsphere excels in high-Q sensing and wavelength selectivity due to its symmetric stability, the microbottle offers superior geometric flexibility for axial mode manipulation and spectral tuning, establishing that both geometries reach their performance peaks at the identified physical boundaries of the low-cost fabrication system.

Table 4 compares the fabrication of both microsphere and microbottle WGM resonator with the other microsphere resonators fabricated using femtosecond lasers [25,26], CO_2 laser [24], and arc discharge [23]. Based on the values, the fabricated microresonators from this work has the diameter that sits in between range with the diameter of microresonators fabricated using CO_2 lasers and arc discharge, significantly larger than those fabricated using femtosecond laser. The Q-factor of the fabricated microresonators sit below than the resonators fabricated using CO2 lasers and arc discharge, moderately within range with those fabricated with femtosecond lasers. The FSR generally is within the nm-scale for all the fabricated resonator.

Table 4. The comparison of the fabricated microsphere resonators with other methods of fabrication

References	Diameter	Q-factor	FSR
This work (Microsphere)	~250 – 260 μm	$1.90x10^4$	2.44 nm
This work (Microbottle)	~230 – 280 μm	$1.38x10^4$	1.40 nm
Kang et al. [23]	~100 – 300 μm	$\geq 10^7$–10^8	nm-scale
Brice et al. [24]	100-500 μm	10^6 – 10^9	nm-scale
Hou et al. [25]	5-25 μm	$\sim 3\times10^3$	~7.46 nm
Lin et al. [26]	~82 μm	2.5×10^5	nm-scale

In summary, while microbottles offer flexibility and tuning potential, microspheres are both easier to fabricate and more consistent under low-cost fusion splicer conditions, while simultaneously providing higher Q factors and larger FSR values. Thus, the diameter limitations observed confirm that microspheres represent a more viable and practical path for low-cost, high-Q resonator fabrication compared to microbottles.

4. Conclusion

This study establishes the diameter limitations and performance boundaries of microsphere and microbottle WGM resonators fabricated using a low-cost fusion splicer. Microspheres are constrained by thermal equilibrium, reaching a saturation diameter of 260.9 μm beyond 30 arc discharges, resulting in high reproducibility (SD = 2.0 μm) and superior optical performance, with a peak Q-factor of 18,894 and an FSR of 2.44 nm. In contrast, microbottle resonators are limited by mechanical failure. The radial diameter exhibits a highly linear and controllable growth, increasing from 193.5 μm at 20 arc discharges to 232.5 μm at 50 arc discharges ($R^2 = 0.9723$). The fabrication process also demonstrates strong reproducibility, with standard deviation decreasing from 4.84 μm to 0.97 μm as the diameter increases. However, the process is restricted to a maximum of 50 discharges, beyond which fiber fracture occurs. Additionally, the microbottle undergoes axial contraction to 484.8 μm due to surface-tension-driven material redistribution. The microbottle has a lower Q-factor (13,843) and reduced FSR (1.40 nm), while providing enhanced flexibility for axial mode control. Overall, the identification of thermal saturation in microspheres and structural limits in microbottles provides a comprehensive framework for optimizing WGM resonator design under low-cost fabrication constraints.

Acknowledgements

We would like to thank the Ministry of Higher Education of Malaysia (MOHE) for providing the grant of FRGS/1/2022/STG07/UIAM/02/1.

References

[1] Y. Chen, Y. Yin, L. Ma, O. G. Schmidt, Advanced Optical Materials **9**(12), 2100143 (2021).
[2] Y. Guo, Y. Liang, Y. Li, B. Tian, X. Fan, Y. He, M. Liu, L. Peng, N. Tang, T. Tan, B. Yao, Advanced Devices and Instrumentation **5**, 0041 (2024).
[3] N. Toropov, G. Cabello, M. P. Serrano, R. R. Gutha, M. Rafti, F. Vollmer, Light: Science and Applications **10**(1), 42 (2021).
[4] S. Hao, J. Su, Reports on Progress in Physics **88**(1), 016402 (2025).
[5] N. A. Baharuddin, N. Mokhtar, H. A. Zain, M. A. M. Johari, R. Apsari, S. W. Harun, Optik **242**, 167328 (2021).
[6] X. Li, D. N. Wang, Journal of Lightwave Technology **39**(11), 3466 (2021).
[7] D. Zurikovs, I. Murans, D. Ortiz, D. Prigunovs, J. Alnis, T. Salgals, S. Marinins, M. Parfjonovs, I. Andersone, V. Bobrovs, Photonics and Electromagnetics Research Symposium-Spring (PIERS-Spring), 1 (2025).
[8] M. Loyez, M. Adolphson, J. Liao, L. Yang, ACS Sensors **8**(7), 2440 (2023).
[9] Y. Hu, Z. Fan, X. Dai, Q. Dai, B. Niu, H. Zhang, G. Jing Fan, Journal of Lightwave Technology **44**(2), 593 (2026).
[10] W. Li, H. Gong, X. He, B. Xu, C. Zhao, C. Shen, IEEE Sensors Journal **25**, 41244 (2025).
[11] Y. Li, H. Wang, Z. Guo, X. Zhao, Y. Zhou, Q. Wang, M. Luo, H. Cai, L. K. Chin, A.-Q. Liu, X. Wu, Microsystems and Nanoengineering **12**(1), 35 (2026).
[12] G. Frigenti, D. Farnesi, S. Berneschi, S. Pelli, G. C. Righini, G. N. Conti, S. S. Huguet, Journal of the European Optical Society-Rapid Publications **21**(1), 26 (2025).
[13] L. Shi, Q. Wang, J. Luo, T. Zhu, Optics and Lasers in Engineering **137**, 106329 (2021).
[14] T. C. Lee, H. Y. Lin, Y. C. Tsao, G. Z. Lu, Y. P. Hsieh, Y. F. Chen, Nanoscale **17**(40), 23511 (2025).
[15] J. Ward, O. Benson, Laser and Photonics Reviews **5**(4), 553 (2011).
[16] S. Yang, Y. Wang, H. Sun, Advanced Optical Materials **3**(9), 1136 (2015).
[17] A. E. Shitikov, I. A. Bilenko, N. M. Kondratiev, V. E. Lobanov, A. Markosyan, M. L. Gorodetsky, Optica **5**(12), 1525 (2018).
[18] Y. Yang, Z. Wang, X. Zhang, Q. Zhang, T. Wang, Frontiers of Optoelectronics **16**(1), 10 (2023).
[19] M. Sumetsky, Optics Letters **45**(15), 4116 (2020).
[20] Y. Wang, Y. Wang, G. Huang, Y. Kong, C. Liu, Z. Zhao, K. Wu, Y. Mei, Advanced Photonics Research **2**(5), 2000163 (2021).
[21] C. He, H. Sun, J. Mo, C. Yang, G. Feng, H. Zhou, S. Zhou, Laser Physics **28**(7), 076202 (2018).
[22] M. Wang, Y. Yang, Z. Lu, W. Wang, W. Zhang, C. Xie, H. Zhong, L. Wu, T. Wu, Q. Tan, Y. Fu, K. Wang, Journal of Lightwave Technology **39**(18), 5917 (2021).
[23] Z. Kang, B. Yang, J. Liu, Y. Wang, D. Tang, L. Zhang, K. Wang, Y. Yang, Iscience **28**(7), 112822 (2025).
[24] I. Brice, V. V. Kim, A. Ostrovskis, A. Sedulis, T. Salgals, S. Spolitis, V. Bobrovs, J. Alnis, R. A. Ganeev, Nanomaterials **13**(13), 1997 (2023).
[25] Z. S. Hou, Q. L. Huang, X. P. Zhan, A. W. Li, H. L. Xu, RSC Advances **7**(27), 16531 (2017).
[26] J. Lin, Y. Xu, Z. Fang, M. Wang, N. Wang, L. Qiao, W. Fang, Y. Cheng, Science China Physics, Mechanics and Astronomy **58**(11), 114209 (2015).

*Corresponding author: mzz@iium.edu.my